

A model of failed solar eruption initiated and destructed by magnetic reconnection

Chaowei Jiang,^{1,2*} Aiyong Duan,³ Peng Zou,¹ Zhenjun Zhou,³ Xinkai Bian,¹ Xueshang Feng,^{1,2} Pingbing Zuo,^{1,2} and Yi Wang^{1,2}

¹*Shenzhen Key Laboratory of Numerical Prediction for Space Storm, Institute of Space Science and Applied Technology, Harbin Institute of Technology, Shenzhen 518055, China*

²*Key Laboratory of Solar Activity and Space Weather, National Space Science Center, Chinese Academy of Sciences, Beijing 100190, China*

³*School of Atmospheric Sciences, Sun Yat-sen University, Zhuhai 519000, China*

Accepted XXX. Received YYY; in original form ZZZ

ABSTRACT

Solar eruptions are explosive disruption of coronal magnetic fields, and often launch coronal mass ejections into the interplanetary space. Intriguingly, many solar eruptions fail to escape from the Sun, and the prevailing theory for such failed eruption is based on ideal MHD instabilities of magnetic flux rope (MFR); that is, a MFR runs into kink instability and erupts but cannot reach the height for torus instability. Here, based on numerical MHD simulation, we present a new model of failed eruption in which magnetic reconnection plays a leading role in the initiation and failure of the eruption. Initially, a core bipolar potential field is embedded in a background bipolar field, and by applying shearing and converging motions to the core field, a current sheet is formed within the core field. Then, tether-cutting reconnection is triggered at the current sheet, first slow for a while and becoming fast, driving an erupting MFR. Eventually, the rise of MFR is halted by the downward magnetic tension force of the overlying field, although the MFR apex has well exceeded the critical height of torus instability. More importantly, during the rise of the MFR, it experiences a significant rotation around the vertical axis (with a direction contrary to that predicted by kink instability), rendering the field direction at the rope apex almost inverse to the overlying field. As a result, a strong current sheet is formed between the MFR and the overlying flux, and reconnection occurring in this current sheet ruins completely the MFR.

Key words: Sun: Magnetic fields – Sun: Flares – Sun: corona – Sun: Coronal mass ejections – magnetohydrodynamics (MHD) – methods: numerical

1 INTRODUCTION

Solar eruptions, including mainly solar flares and coronal mass ejections (CMEs) have been recognized as a leading driver of disastrous space weather in the solar-terrestrial space environment. Now it is commonly believed that solar eruptions have their root in the evolution of magnetic fields in the solar atmosphere, in particular, the solar corona where magnetic fields dominate the dynamics. Although not being directly observed, the coronal magnetic fields in three-dimensional configuration have a high degree of complexities as inferred from the plasma emissions (Aschwanden 2004), and it remains elusive how the solar eruptions are initiated. One of the complexities is reflected in an interesting fact that solar eruptions can be classified into two distinct types, namely eruptive flares and confined flares. In eruptive flares, the eruption structures (plasma and magnetic flux) can successfully escape into the solar wind and form the so-called

interplanetary CMEs. The confined flares are those without association of CME, and they appear to be further divided into two types. In some confined flares, only a series of brightening of coronal loops are observed without much change in their shape during the flare, for example in the well known X-class confined flares in the super active region (AR) NOAA 12192 (Sun et al. 2015; Jiang et al. 2016). In other confined flares, the impulsive phase is similar to the eruptive flares in that there are evident fast acceleration of magnetic structures, i.e., erupting filaments, to certain heights, but the erupting structures are quickly decelerated by some reasons and fail to escape as a CME, and these events are known as failed filament eruptions (Ji et al. 2003; Zhou et al. 2019; Filippov 2020). Therefore to understand these failed eruptions, one should know how the magnetic field is first initiated to rise impulsively and then how it is trapped.

A prevailing model for failed eruption is that a coronal magnetic flux rope (MFR) runs into kink instability but does not reach the threshold height for torus instability (Török & Kliem 2005; Hassanin & Kliem 2016; Hassanin et al. 2022).

* E-mail: chaowei@hit.edu.cn (CWJ)

MFR refers to a coherent group of magnetic field lines winding around a common axis, and is believed to a fundamental magnetic configuration in solar eruptions (Cheng et al. 2017; Guo et al. 2017; Liu 2020; Patsourakos et al. 2020; Duan et al. 2019). The kink instability occurs when the twist degree of field lines exceeds a certain threshold, and during its development, the MFR axis will be deformed with the increase of its writhe at consumption of the magnetic field line twist (Hood & Priest 1979, 1981; Török et al. 2004, 2010; Török & Kliem 2005). As a result, the MFR will rise rapidly. It can erupt successfully if the apex of the axis reaches a critical height above which the overlying field decays sufficiently fast with height. In such case, another instability due to the interaction of the MFR and its strapping field, known as the torus instability (Kliem & Török 2006; Démoulin & Aulanier 2010; Aulanier et al. 2010; Fan 2010), is triggered. Otherwise the erupting MFR will not be able to break through the strong overlying field and thus results in failed eruption. Both these two cases, i.e., the successful eruption and failed eruption, have been shown by Török & Kliem (2005) using MHD simulation with initial condition given by a MFR model developed in Titov & Démoulin (1999).

In this paper, we proposed a new model of failed eruption in which magnetic reconnection plays the major role in the initiation and failure of the eruption. This model is developed based on our recent numerical simulations of a fundamental mechanism of eruption initiation (Jiang et al. 2021, referred to as Paper A in the following) and also in (Bian et al. 2022c,b), in which a successful eruption can be triggered and driven by fast reconnection at a current sheet that is formed in the quasi-static evolution of a continually-sheared magnetic arcade. In this work, we show that the eruption as initiated by the reconnection can be failed by adding an overlying field with sufficient strength to the sheared arcade (which is referred to as the core field). After the current sheet is formed in the core field as driving by shearing and converging motions, there is a short interval with slow reconnection at the current sheet, through which a MFR is created. Then the reconnection becomes fast, and the MFR rises impulsively, marking the onset of eruption. At the eruption onset, there is no evidence for either kink instability or torus instability of the MFR, and the Lorentz force analysis shows that the acceleration of the MFR is driven by the slingshot effect of the reconnection. Eventually, the rise of MFR is halted by the downward magnetic tension force of the background overlying field, although the MFR apex has well exceeds the critical height of torus instability. More importantly, during the rise of the MFR, the interaction of the MFR with the background field renders a fast rotation of the MFR around the vertical axis (with a direction inverse to that as predicted by the kink instability) until its direction at the apex of the rope is almost inverse to the overlying field. As a result, a strong current sheet is formed between the MFR and the overlying flux and reconnection occurs in this current sheet ruins completely the MFR.

2 METHOD

The model is developed based on numerically solving the full set of MHD equations with typical plasma and magnetic field settings for the corona, which is essentially an

environment with low plasma β , very low resistivity and viscosity (corresponding to very high Lundquist and Reynolds numbers), and high ratio of Alfvénic to sonic speeds. As the specific form of the equations has been given in Paper A, we will not repeat it here. The variables are all non-dimensionalized by typical values in the corona, which are respectively, length $L_s = 11.52$ Mm, and time $t_s = 105$ s, density $\rho_s = 2.29 \times 10^{-15}$ g cm $^{-3}$, temperature $T_s = 10^6$ K, velocity $v_s = 110$ km s $^{-1}$, magnetic field $B_s = 1.86$ G. The computational volume spans a large Cartesian box with both x and y extending $[-32, 32]$ and $z \in [0, 64]$ (all the values are expressed in non-dimensionalized numbers in this paper if not mentioned particularly). The full volume is resolved by a block-structured adaptive mesh refinement (AMR) grid in which the highest resolution is $\Delta = 1/64$ (corresponding to 180 km) to capture the formation process of the current sheet and the reconnection in the core field. The bottom surface of the computational volume (the $z = 0$ plane), which mimics the photosphere, is assumed to be a line-tied boundary at which the footpoints of the coronal magnetic field are anchored and convect with a prescribed surface flow. At the bottom boundary, we directly solve the magnetic induction equation to self-consistently update the magnetic field as driven by the surface flow (which is implemented in the same way as Paper A). All other boundaries are open and nonreflecting by zero-gradient extrapolation of variables from their neighboring inner points. Same as Paper A, we chose to not use explicit resistivity in the magnetic induction equation, but magnetic reconnection can still be triggered through numerical diffusion when a current layer is sufficiently narrow (which supports a sufficiently strong current density) with thickness close to the grid resolution. By this, we achieved an effective resistivity as small as we can with given grid resolutions. Such setting also mimics the current-density-dependent resistivity as required for fast Petscheck-type reconnection.

At the beginning, a magnetic flux distribution at the bottom surface, $B_z(x, y, 0) = B_c + B_g$, is given by the superposition of a core bipole B_c and a background bipole B_g , both of which have the same form defined as

$$B_i = b_i e^{-x^2/\sigma_i^2} (e^{-(y-y_i)^2/\delta_i^2} - e^{-(y+y_i)^2/\delta_i^2}), \quad (1)$$

where the subscript i denotes c or g . For the core bipole $\sigma_c = 2$, $\delta_c = 1$, $y_c = 0.1$, and $b_c = 117.4$ is a scaling factor such that the maximum of B_c is 20, and for the background bipole $b_g = 10$, $\sigma_g = 4$, $\delta_g = 2$, $y_g = 6$. The core field is a compact bipole, as shown in Figure 1A, while the background field is a dispersed bipole with much larger extents (Figure 1B). The ratio of unsigned fluxes between the core field and the background field is 0.33. Then, a potential field is calculated for the bottom flux distribution using the Green's function method. With this potential field and a plasma in hydrostatic equilibrium as the initial condition, we drive the MHD system to evolve using surface motion at the lower boundary (i.e., driving motion). We have carried out two simulations, one simulation (with both the core field and the background field) that produced a failed eruption, and the other with only the core field that can produce successful eruption. The simulations consists of different phases, which are respectively the shearing phase, the converging phase, and the non-driving phase, as defined by different driving motion. In the shearing phase, we use a rotational flow applied to each of the two magnetic polarities in the core field. The velocity is defined

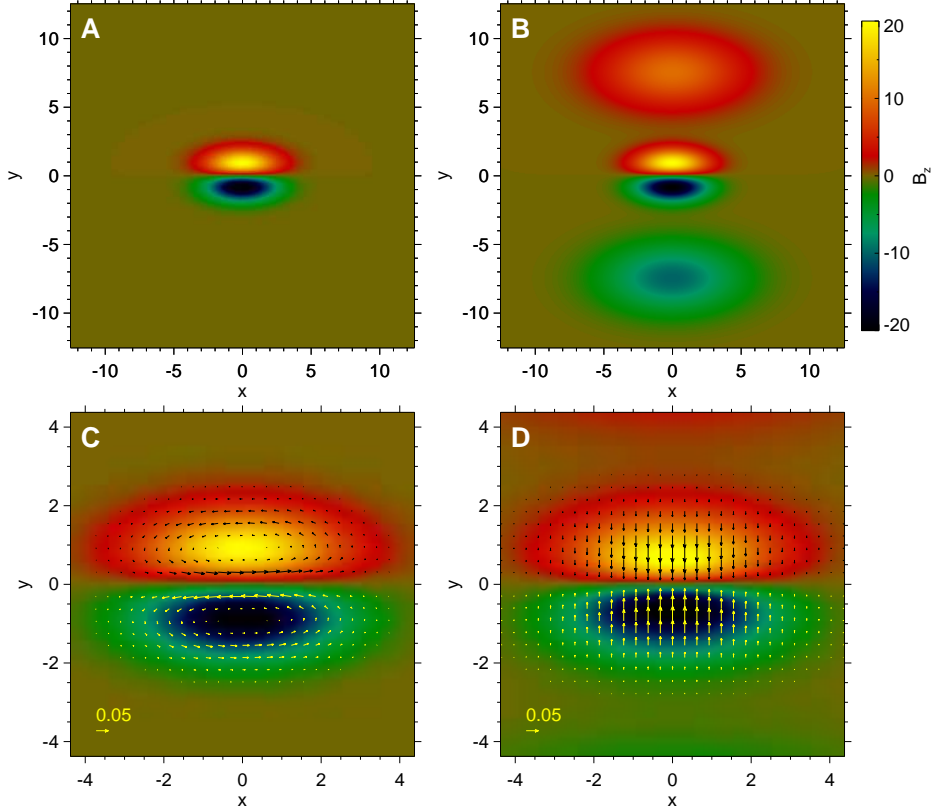


Figure 1. Magnetic flux distribution and driving flow at the bottom surface. (A) The case with only the core field. (B) The case with the core field and the background field. (C) Arrows show the surface rotational flow. (D) The surface converging flow.

by

$$(v_x, v_y) = \left(\frac{\partial \psi}{\partial y}, -\frac{\partial \psi}{\partial x} \right); \psi = r_0 B_c^2 e^{-(B_c^2 - B_{c,\max}^2)/B_{c,\max}^2}, \quad (2)$$

where $B_{c,\max}$ is the largest value of the B_c and r_0 is a constant for scaling such that the maximum of the surface velocity is 0.06. This rotational flow will not modify the flux distribution at the bottom surface. In the converging phase, we apply a converging flow to the core field, defined as

$$(v_x, v_y) = (0, -c_0 B_c) \quad (3)$$

where c_0 is also a constant for scaling such that the maximum of the surface velocity is 0.06. This can drive the flux towards the PIL and help to build up a current sheet above the PIL. In the non-driving phase, we stop all the driving motion and let the system to evolve spontaneously. This can test whether the system has reached a critical phase of eruption initiation.

3 RESULTS

3.1 Evolution of energies

Figure 2 shows temporal evolutions of the total magnetic energy E_M , the total kinetic energy E_K and the maximal velocity v_{\max} in the different phases of the simulations. The sharp variation of the maximal velocity with time can indicate the onset of reconnection, since magnetic reconnection can impulsively accelerate the plasma. The results are shown for both the simulation of only the core field (Figure 2A and B) and

the one with the core field embedded in the background field (Figure 2C and D). The values of all the energies are normalized by the potential field energy of the core field (named as E_0). In both simulations, the evolution of magnetic energy consists of two distinct stages, a slow accumulation stage and a fast release stage. The transition point of the two stages marks the onset of eruption, which is $t = 78$ in the simulation with only the core field and $t = 104$ in the simulation with the background field. In the pre-eruption stage, the MHD system evolves in a quasi-static way, since the kinetic energy keeps a very low level of mostly below $10^{-3} E_0$. While with the onset of the eruption the kinetic energy impulsively increases, reaching a peak value of around $10^{-1} E_0$. The behaviors after then are rather different between the two cases. In the case with only the core field, the kinetic energy keeps unchanged until the eruptive structure hits the side/top boundaries of the computational volume, and then decreases because the eruption leaves the volume freely. This shows that the eruption is successful. In contrast, the kinetic energy in the case with the background field rapidly declines, with a majority part (only 75%) lost before any disturbance reaching the numerical boundaries, which shows that the eruption is failed and trapped within the computational volume.

3.2 Simulation with no background field

For the simulation with only the core field, its eruption is produced by applying the continuous shearing at the bottom surface until the eruption onset time. The eruption is

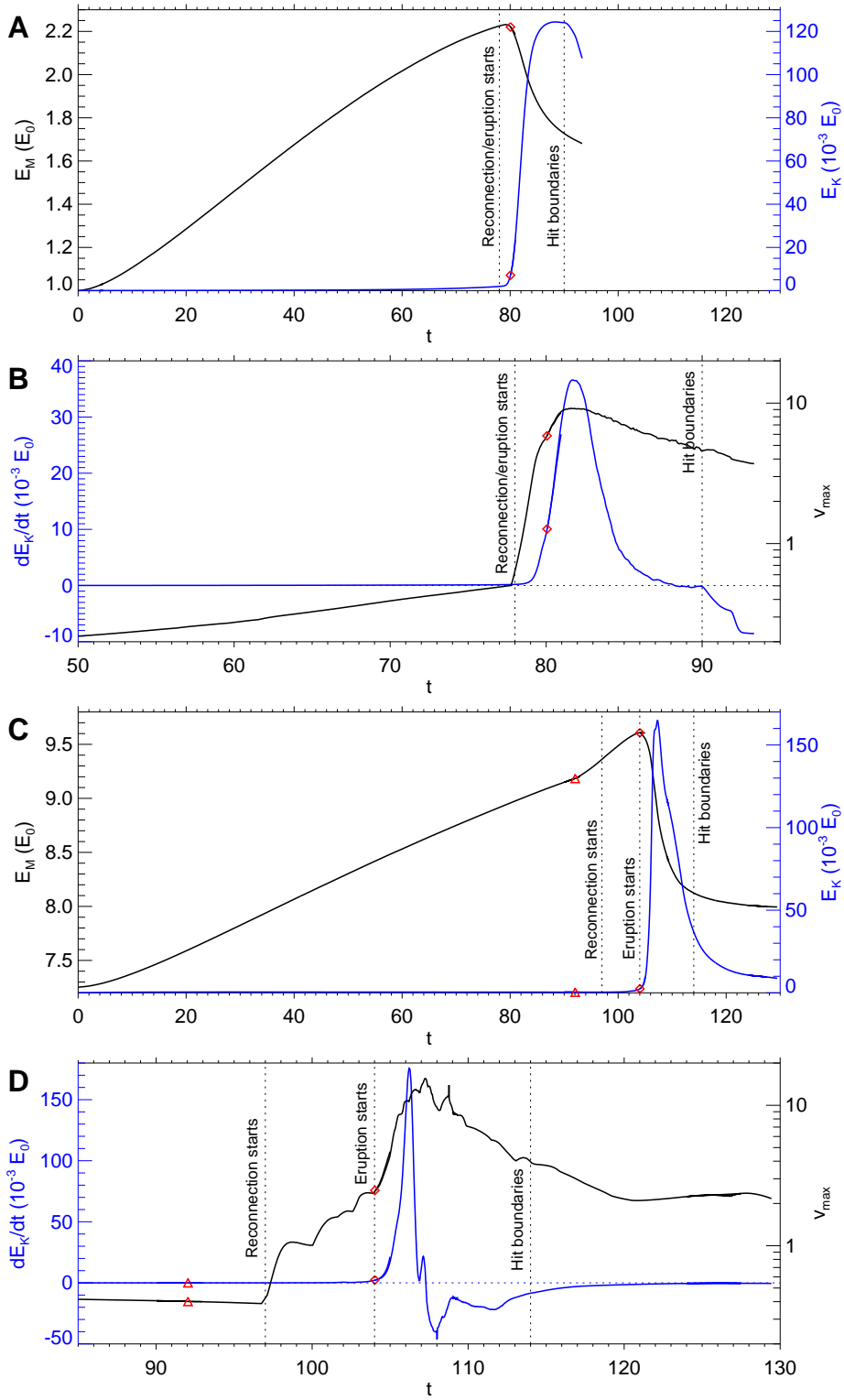


Figure 2. Temporal evolution of energies and velocity in the simulations. (A) Magnetic and kinetic energies in the case with only the core field. The energies are normalized by the potential field energy of the core field. (B) Time derivative of the kinetic energy and the maximal velocity in the case with only the core field. Note that the axis of the velocity is shown in logarithm scale for emphasizing its rapid changes with onset of reconnection. (C) and (D) have the same format with that of (A) and (B) respectively, but for the case with the background field. In the panels, the diamond symbol colored in red indicates that the surface driving is turned off. The triangle symbol in red indicates that the shearing motion is turned off and the converging motion is turned on. The critical stages are denoted by the vertical dashed lines, which include the start of reconnection, the onset of eruption and the time when the eruptive disturbances reach the lateral/top boundaries.

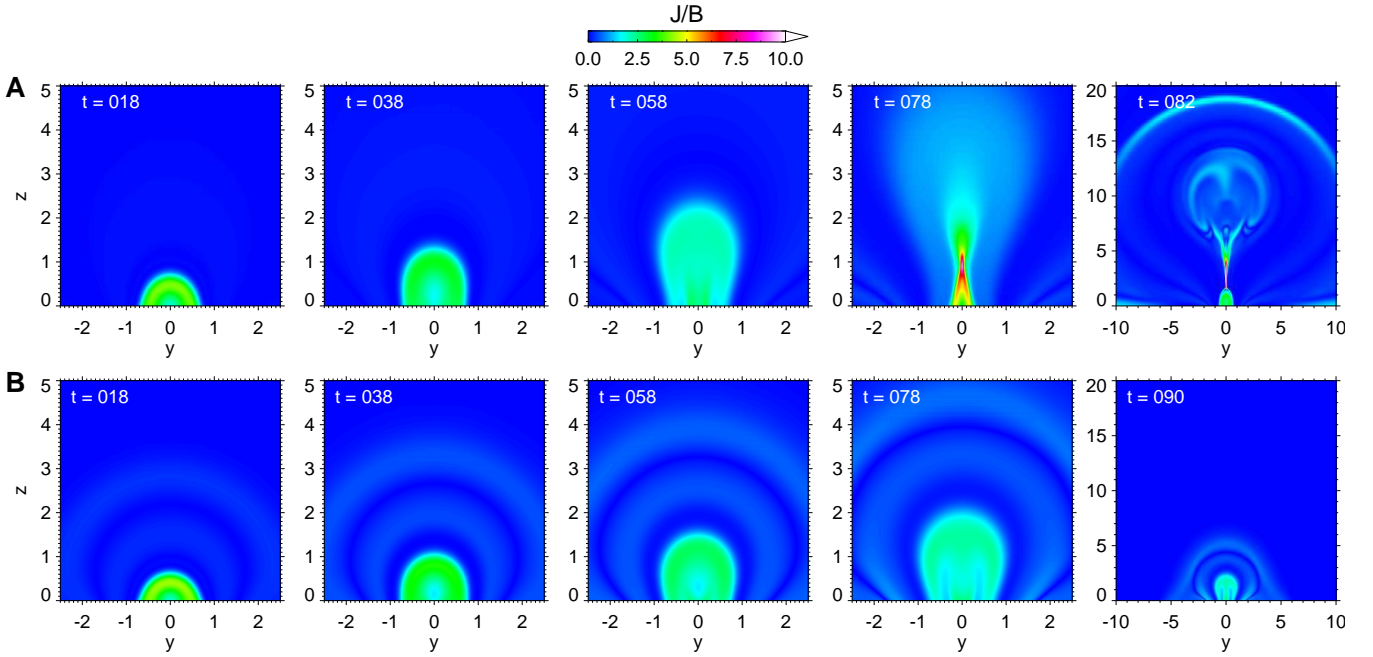


Figure 3. Comparison of the current distribution in the central vertical slice (i.e., the $x = 0$ plane) for two simulation cases in the shearing driving phase. (A) The case with only the core field which produces a successful eruption. Note that at around $t = 78$ a current sheet is formed, and then the eruption is immediately triggered by reconnection at the current sheet. (B) The case with the background field. No current sheet is formed even the shearing driving is applied until $t = 90$.

initiated through the same mechanism as demonstrated in a series of our previous studies (Paper A, and [Bian et al. 2022b,c,a](#)). That is, through quasi-statically surface shearing motion along the PIL, a vertical current sheet forms slowly above the PIL, and once the current sheet is sufficiently thin such that ideal MHD is broken, reconnection sets in and immediately triggers the eruption (see Figure 3A, and also the detailed analysis of Paper A). In Paper A, it is also confirmed that the reconnection results in a strong upward tension force which plays the key role in driving the eruption, that is, the slingshot effect of the reconnection is the main driver of the eruption (see the last section in Methods of Paper A). We note that this mechanism is different from the tether-cutting eruption initiation model ([Moore et al. 2001](#)) in a twofold sense. Firstly, the tether-cutting model is a two-step reconnection process, in which it is assumed that before the onset of the eruption (i.e., the start of impulsive phase of eruption), there is a phase of slow reconnection from more than ten minutes to a few hours, which gradually cuts the tethers, and it is not until a “global instability” occurs that the eruption can start. Secondly, the tether-cutting model proposed that the reconnection only plays the role of cutting the confinement of the field lines and it is the unleashed magnetic pressure that drives the eruption.

3.3 Simulation with background field

For the case with the background field, no eruption is resulted during the shearing phase (which is applied until $t = 92$), since the current sheet has not yet formed, as shown in Figure 3B. The reason is that, due to the constraining effect of the overlying background field, the core field cannot stretch

outward sufficiently like the case without the background field (compare Figure 3B with A). In principle, a current sheet can eventually form if a sufficiently large amount of free energy is injected into the system, such that the total magnetic energy is close to that of a fully open field, but this might not be realized by only shearing the core field using the rotational flow. Then to create a current sheet more efficiently, we apply the converging motion to the core field starting from $t = 92$. The converging flow injects magnetic energy into the corona with a faster rate than the shearing motion (Figure 2C). Figure 4 shows that, by the converging flow, the core field is compressed towards to the PIL, and consequently a current sheet forms at around $t = 97$, with a lower height than that in the case with only the core field.

Subsequently, reconnection is triggered at the current sheet, as shown by the topology change of the core field from sheared arcade to flux rope (Figure 4B) and the reconnection flows (Figure 4C). The start of reconnection is also indicated by the sudden rise of the maximal velocity as shown in Figure 2D, at $t = 97$. But interestingly, unlike the case without the background field, this reconnection does not immediately initiate an eruption because the stabilizing effect of the overlying flux. The reconnection occurs slowly as the Alfvénic Mach number of the reconnection outflow is mostly smaller than 0.1 before $t = 104$. This actually is line with the first step reconnection of the tether-cutting model, i.e., the slow reconnection phase, which creates a stable MFR. The slow reconnection takes a short interval from $t = 97$ to 104, and during this interval, the maximal velocity v_{\max} shows also an intermittent increase and decrease, maintaining within a low level of up to 2 (Figure 2D), which reflects the fact that the reconnection is confined by the overlying field. This is clearly

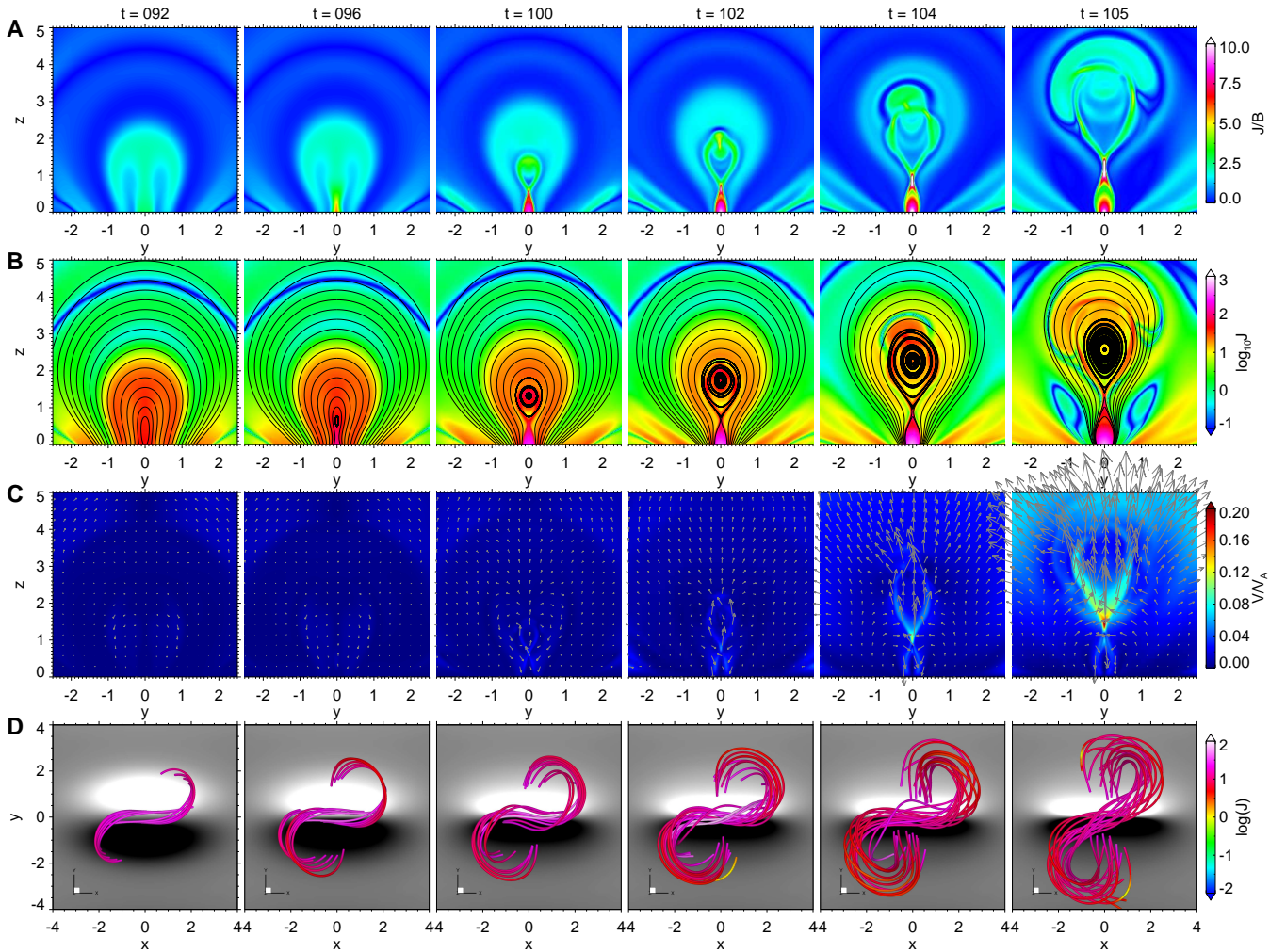


Figure 4. Formation of a pre-eruption MFR by slow tether-cutting reconnection until the eruption onset in the simulation of the failed eruption. (A)–(C) shows the current density normalized by magnetic field (J/B), the current density, and the Alfvénic Mach number on the central vertical slice (the $x = 0$ slice). In (B), the curves show the projection of the magnetic field lines on the slice. In (C), the arrows denote the velocity. (D) Sampled magnetic field lines showing the transformation from the sheared arcade to the MFR. The color of the field lines indicates the current density. The background shows the magnetic flux distribution at the bottom boundary.

different from the case with only the core field, in which the reconnection becomes fast once starts as the v_{\max} impulsively rises to Alfvénic speed of close to 10 (Figure 2C). After the stage of slow reconnection, an eruption starts with continual and fast rise of the v_{\max} to also an Alfvénic value. Figure 5 shows the eruption of the MFR and its final breaking up during its interaction with the background field.

3.4 Ideal instabilities of the pre-eruption MFR

To check whether the eruption is triggered by the torus instability of the MFR, in Figure 6 we traced the apex height of the axis of the MFR and calculated the decay index of the potential field (which approximates the strapping field of the MFR). The decay index is defined as $n(z) = -\partial(\ln B)/\partial \ln z$ along the z axis. As can be seen in Figure 6A, the MFR experiences a slow rise from around $z = 1$ to 2 before the eruption, as driven by the slow reconnection. Once the eruption begins, it rises rapidly to a peak height of around $z = 20$

and then breaks up (due to reconnection with the background field, to be analyzed below). After the MFR breaks up, the height is recorded for apex of the field line rooted in the footpoints of the original MFR axis. Figure 6B shows that from the pre-eruption to the early phase of the eruption (until $t = 105$), the decay index at the apex of the MFR axis is $n = 1 \sim 1.1$. This value is lower than the canonical threshold (1.5) of torus instability, and also below the typical unstable range of 1.5 ± 0.2 as derived in many theoretical and numerical studies (e.g., Kliem & Török 2006; Fan & Gibson 2007; Aulanier et al. 2010; Zuccarello et al. 2015) as well as statistical observational studies (Duan et al. 2019, 2021), which suggests that the eruption is not initiated by torus instability. Note that from $t = 100$ to 104, the decay index shows a mild decrease although the MFR rises. This is because the height profile of the decay index has a saddle-like shape (Luo & Liu 2022) with the transition point at around $n = 1 \sim 1.1$, as can be seen in Figure 6C.

When seen from above (Figure 5D), the MFR axis initially

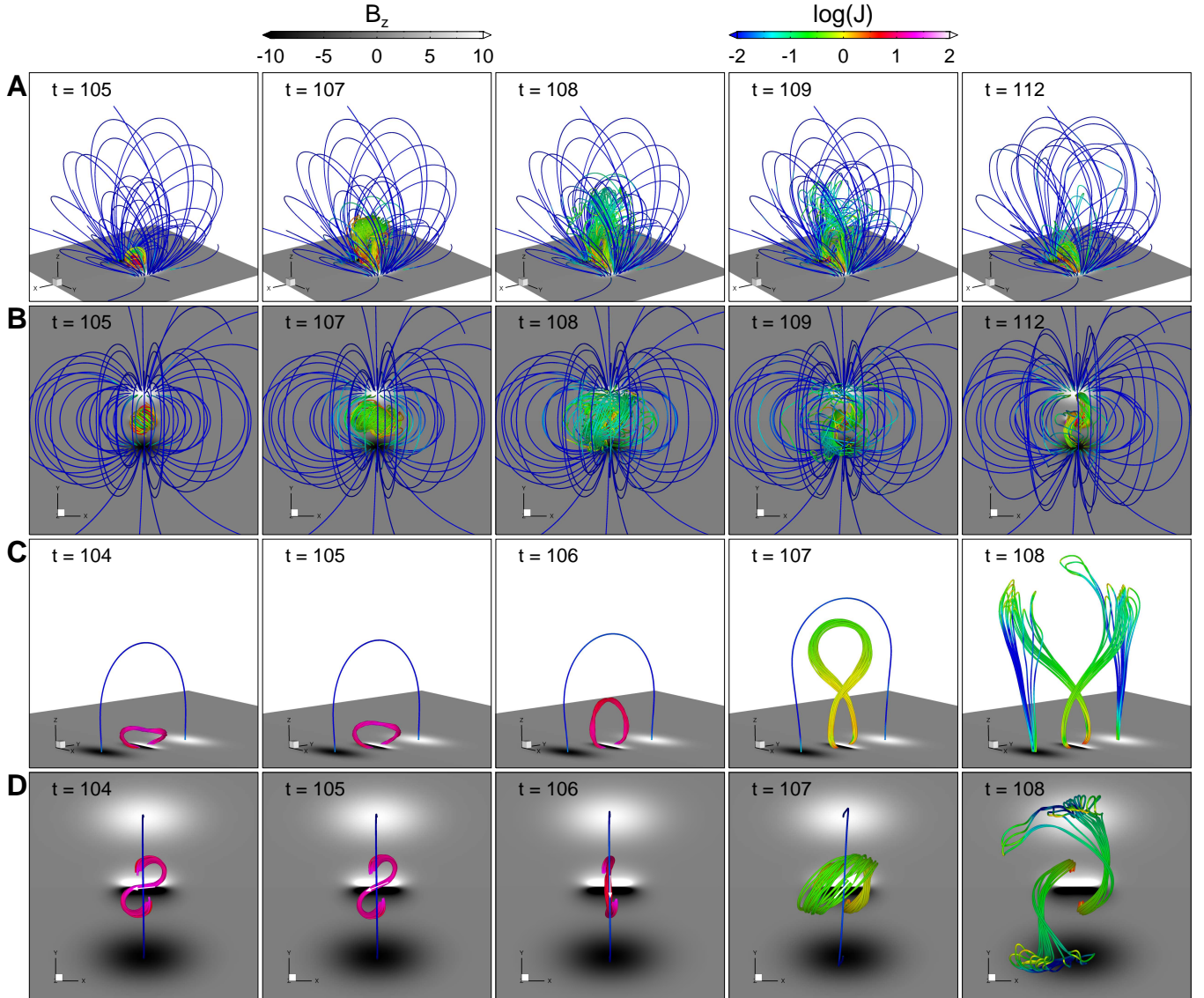


Figure 5. Evolution of magnetic field lines in the failed eruption. (A) 3D prospective view of field lines in the full region. The field lines are pseudo-colored by the current density. The bottom surface is shown with the magnetic flux distribution B_z . (B) Same as (A) but viewed from the top. (C) Close view of the erupting MFR. A field line of the background field is shown. (D) Same as (C) but viewed from the top. The arrows show the direction of the magnetic field lines of the MFR. All the field lines are shown with one of their footpoints fixed on the bottom surface, since no surface motion is applied during the eruption stage. An animation is available for this figure.

has an inverse S shape with its middle part aligned with the PIL. While during the eruption, it undergoes a fast counterclockwise rotation. For instance, at $t = 106$, which is the peak time of acceleration of the eruption (see Figure 2D), it has rotated by nearly 90° and is thus straightened overall, becoming perpendicular to the PIL. The transformation of an erupting MFR from a reversed S to a straight shape indicates a decrease of the writhe of the MFR, which excludes the kink instability of the MFR. Otherwise, the writhe should increase since the kink instability converts magnetic twist into the writhe of the MFR axis. The counterclockwise rotation of the erupting MFR with initially a reverse S shape also occurs in the successful eruption without the background field, which has been carefully studied by Zhou et al. (2022) based

on the simulation in Paper A. They found that this rotation is consistent with the rotation of a typical filament eruption observed from dual viewing angles. Furthermore, by analyzing the Lorentz force and torque, Zhou et al. (2023) confirm that the external shear-field component rather than the internal force of the MFR plays a key role in driving the counterclockwise rotation.

3.5 Driver of the eruption

Here, same as the finding in Paper A, the eruption is initiated by reconnection, and in particular, driven by the strong upward tension force of the newly reconnected field lines. To illustrate this, in Figure 7 we show the upward acceleration

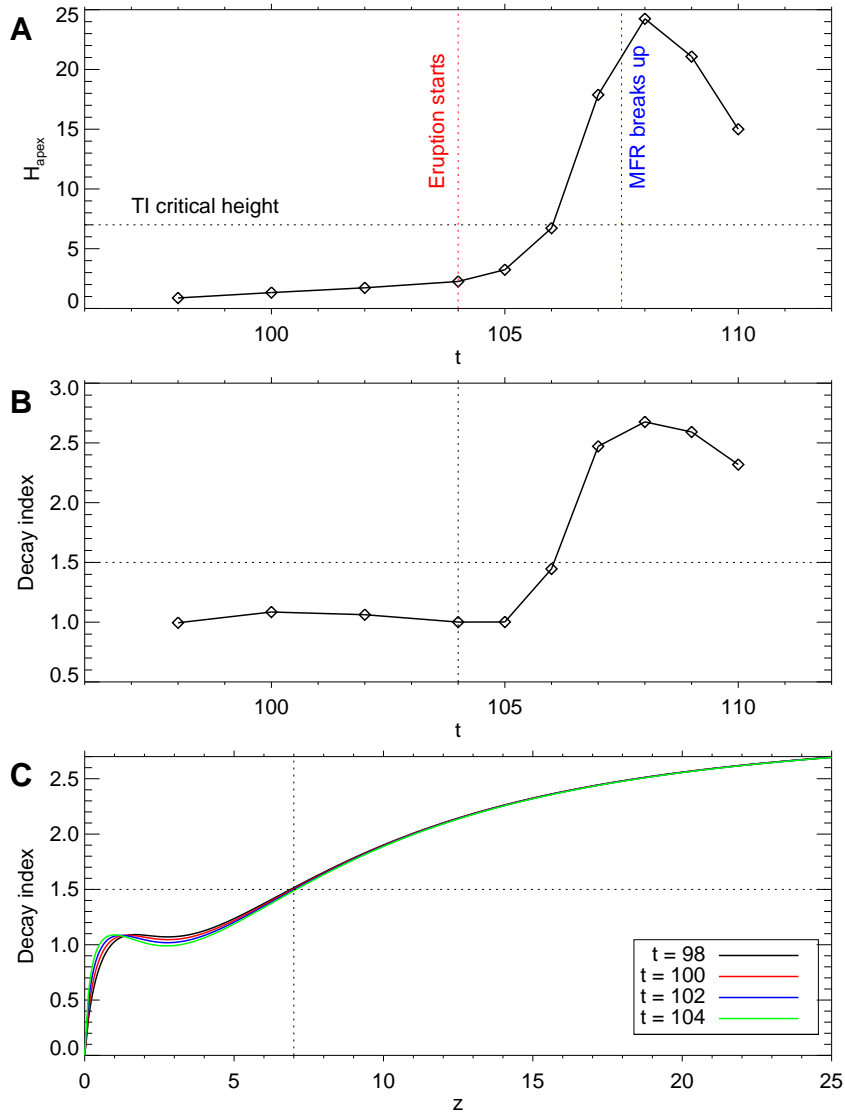


Figure 6. Evolution of the height and decay index of the MFR axis. (A) Temporal evolution of the apex height of the MFR axis. Since the MFR breaks up after $t = 107$, the height is recorded for apex of the field line rooted in the footpoints of the original MFR axis. (B) The decay index of the potential field at the apex of the MFR axis. (C) The height profiles of the decay index during the evolution. Note that the converging motion at the bottom surface changes the magnetic flux distribution and thus the decay index also varies with time. The height and value of the critical decay index $n = 1.5$ are shown by the dashed lines.

by the Lorentz force F_z/ρ on the central vertical cross section of the volume and the profiles of the two force components (the magnetic pressure-gradient force P_z/ρ and tension force T_z/ρ) on the central vertical line from pre-eruption to the peak time of acceleration of the eruption. The slices show that the upward acceleration by the Lorentz force is mainly distributed on the edge of the expanding MFR, i.e., in the newly reconnected flux that joins in the MFR, while the acceleration at the core of MFR is very weak (F_z/ρ is almost zero). In particular, the strongest upward acceleration always resides in the reconnecting current sheet and acts as the central engine of eruption. By decomposing the force into magnetic tension force and pressure-gradient force on the central vertical line, one can see that it is always the magnetic tension force at the reconnecting outflow region of the current sheet (i.e., the slingshot effect of reconnection) that plays

the role of upward acceleration. Since only in this region, the tension force (the blue curve) is not balanced with the pressure-gradient force (the red curve), while elsewhere they almost cancel out with each other. Such unbalance is directly caused by the reconnection which starts at $t = 97$, since before that the forces are perfectly balanced everywhere, see $t = 92$ and 96 in Figure 7. In the early stage of the reconnection, the force unbalance is rather weak (see $t = 98, 100,$ and 102) and is not able to drive a fast eruption, because the newly reconnected field lines will experience a quick deceleration by the downward magnetic pressure-gradient force in the region between the top of the reconnection outflow and the MFR axis. Therefore, the slow reconnection proceeds in this stage, until the force unbalance is sufficiently large to result in a disruption with a fast reconnection. At the peak time ($t = 106$), the acceleration of the slingshot effect is ex-

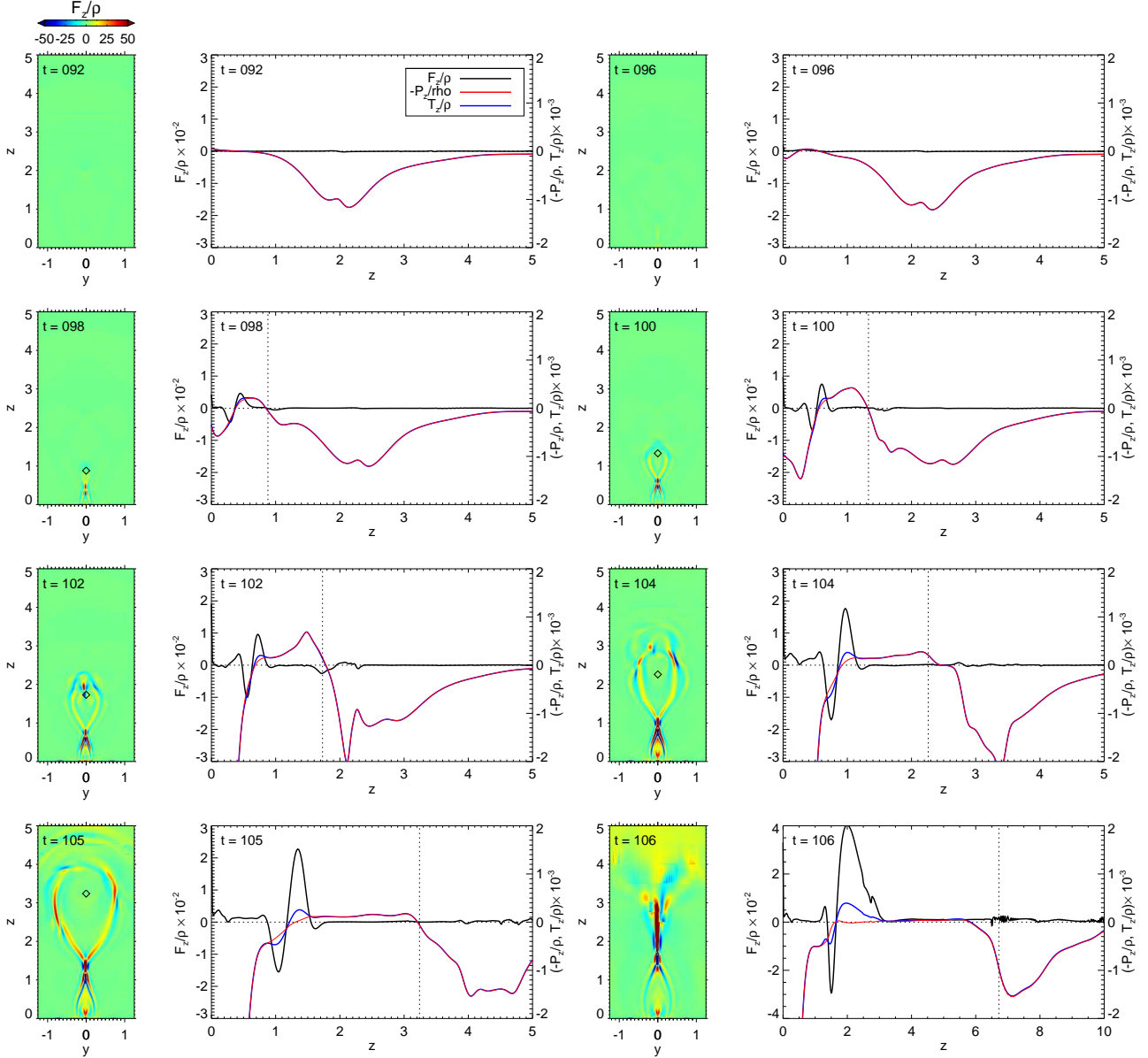


Figure 7. Distribution and evolution of the vertical Lorentz force. For each time, the central vertical slice is shown with the distribution of the vertical acceleration by the Lorentz force F_z/ρ , and the profiles along the central vertical line (i.e., the z axis) are shown for the F_z/ρ (the black line), the magnetic pressure-gradient force P_z/ρ (the red line), and the magnetic tension force T_z/ρ (the blue line). Note that $-P_z/\rho$ is plotted for a better comparison of its magnitude with that of T_z/ρ . Thus when the red and blue lines coincide, the two force components balance each other and F_z/ρ is zero. The diamond symbols on the slices denote the location of the MFR axis, and its height is also shown by the vertical dashed lines in the line plots.

tremely rapid, reaching up to $a_z \approx 200$ (which corresponds to $\sim 200 \text{ km s}^{-2}$) within a height range of $L_z \approx 1$. Thus, as the field line approaches the current sheet and reconnects, its middle point can be accelerated upward to a velocity of around $\sqrt{2a_z L_z} = 20$ (which is consistent with the largest speed as shown in Figure 2D).

3.6 Cause of failure of the eruption

From the time profile of the decay index (Figure 6B), it seems that the MFR enters into the domain of torus instability after

$t = 106$ (during the eruption) and reaches a peak height of ~ 20 with decay index of ~ 2.5 , far above the torus instability threshold. Nevertheless, it does not erupt successfully owing two reasons. Firstly, the erupting flux rope is decelerated by the downward magnetic tension force of the background field overlying the core field. Figure 5C and Figure 8 show that when the erupting MFR reaches the height of ~ 20 , the background field is strongly pushed upward, which in turn results in downward tension force, and consequently the velocity decreases quickly. Secondly, as the MFR rotates about the z axis significantly during its eruption, the field lines at

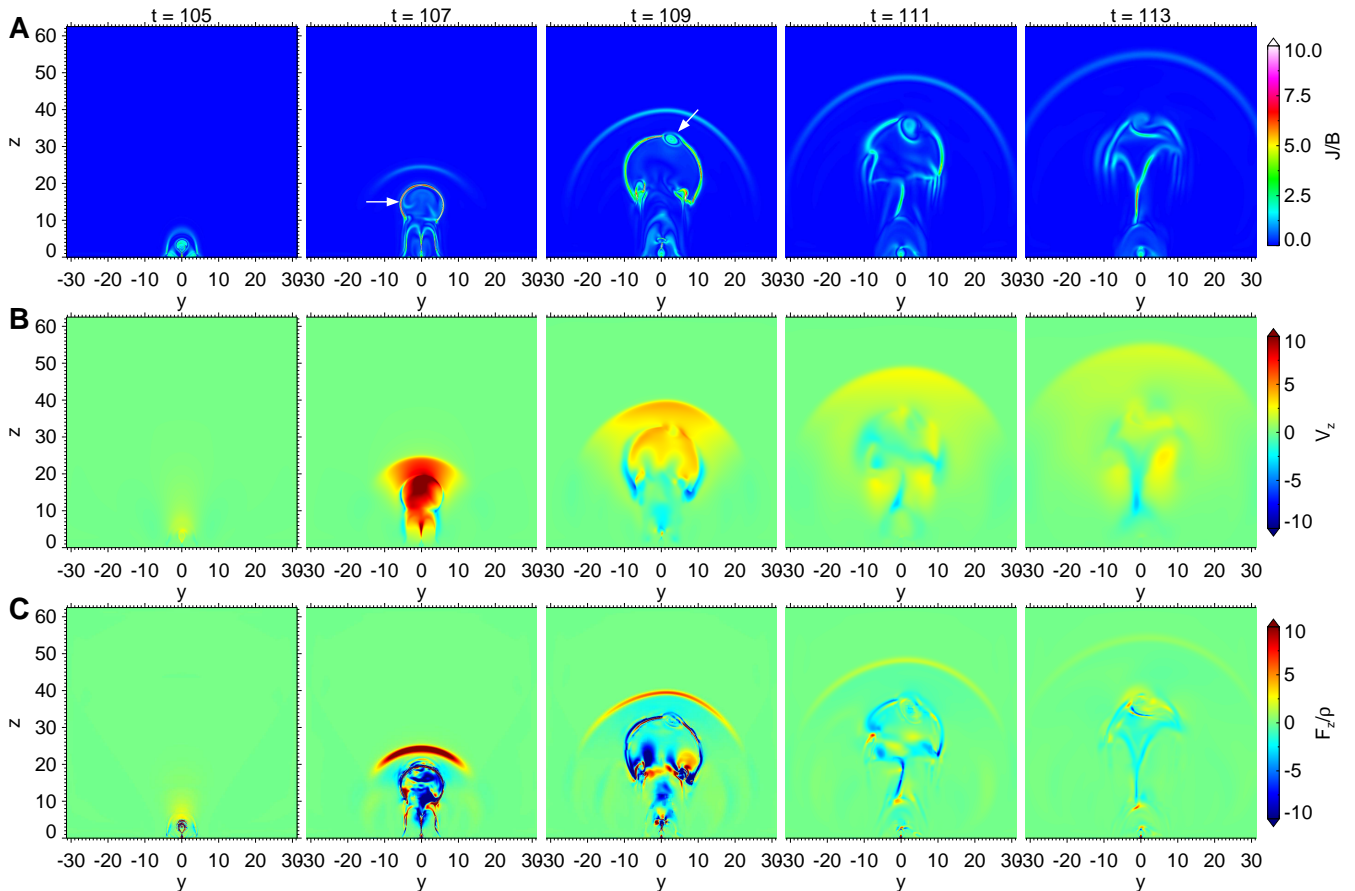


Figure 8. Evolution of different parameters on the central vertical slice of the failed eruption. (A) Current density normalized by the magnetic field strength. (B) Vertical component of the velocity. (C) Vertical component of the Lorentz force. The two arrows denote the external current sheet, and the plasmoid in the current sheet, respectively. An animation is available.

its apex are even reversed in direction to that of the overlying field (Figure 5D). As a result, a strong current sheet is formed between the MFR and the overlying flux (see $t = 107$ in Figure 8A), and reconnection occurs in the current sheet, which destructs the MFR eventually into two arcades connecting both the core and the background polarities (see Figure 5C and D). Interestingly, as this current sheet is rather large in scale, a plasmoid instability is triggered and thus a new small flux rope is formed in the current sheet during the reconnection (see the panel of $t = 109$ in Figure 8A).

4 DISCUSSIONS

We have presented a model for failed solar eruption based on numerical MHD simulations of an eruptive core field embedded in a large-scale background field. This simulation extends a fundamental mechanism of eruption initiation as demonstrated in Paper A to failed eruption. In the model, magnetic reconnection has fundamental importance for formation of a pre-eruption MFR, initiation of its eruption and cause of its failure in producing a CME. The MFR is created by slow tether-cutting reconnection at the current sheet that is formed in the core field as driven by photospheric shearing and converging flows. The eruption, as indicated by fast rise

of the MFR, is caused by reconnection that becomes progressively faster in the core field. The failure and broken up of the erupting MFR is also owing to reconnection, but is an external type which occurs in the interface between the MFR and the overlying field. Our model can explain well the observations of Zhou et al. (2019) that some failed filament eruptions, although with the erupting filament reaching well above the torus-unstable heights, often has a large rotation during its rise. This is because the large rotation of the MFR (i.e., the filament) can result in large angle between the MFR field lines and the overlying ones. Therefore an external current sheet can be formed between the upward rising MFR and the overlying flux and reconnection occurs in this current sheet can ruin the MFR. Such an external reconnection also occurred in the simulations of Hassanin & Kliem (2016) and Chen et al. (2023), in which an ideally unstable MFR (of either kink instability or torus instability) erupts and interacts with the background field through reconnection. In future works, we will investigate what are the key conditions in determining the failure of the eruption, with numerical experiments by using background fields in the parameter space of different strengths, different flux distributions, different flux ratios as well as different angles between them and the core field.

ACKNOWLEDGEMENTS

This work is jointly supported by Shenzhen Science and Technology Program (Grant No. RCJC20210609104422048), Shenzhen Technology Project JCYJ20190806142609035, Shenzhen Key Laboratory Launching Project (No. ZDSYS20210702140800001), Guangdong Basic and Applied Basic Research Foundation (2023B1515040021) and National Natural Science Foundation of China (NSFC 42174200). The computational work was carried out on TianHe-1(A), National Supercomputer Center in Tianjin, China.

DATA AVAILABILITY

All the data generated for this paper are available from the authors upon request.

REFERENCES

- Aschwanden M. J., 2004, *Physics of the Solar Corona. An Introduction*. Springer Praxis Books
- Aulanier G., Török T., Démoulin P., DeLuca E. E., 2010, *The Astrophysical Journal*, 708, 314
- Bian X., Jiang C., Feng X., 2022a, *Frontiers in Astronomy and Space Sciences*, 9, 982108
- Bian X., Jiang C., Feng X., Zuo P., Wang Y., Wang X., 2022b, *Astronomy & Astrophysics*, 658, A174
- Bian X., Jiang C., Feng X., Zuo P., Wang Y., 2022c, *The Astrophysical Journal Letters*, 925, L7
- Chen J., Cheng X., Kliem B., Ding M., 2023, A Model for Confined Solar Eruptions Including External Reconnection (arxiv:2306.04993)
- Cheng X., Guo Y., Ding M., 2017, *Science China Earth Sciences*, 60, 1383
- Démoulin P., Aulanier G., 2010, *The Astrophysical Journal*, 718, 1388
- Duan A., Jiang C., He W., Feng X., Zou P., Cui J., 2019, *The Astrophysical Journal*, 884, 73
- Duan A., Jiang C., Zhou Z., Feng X., Cui J., 2021, *The Astrophysical Journal*, 907, L23
- Fan Y., 2010, *The Astrophysical Journal*, 719, 728
- Fan Y., Gibson S. E., 2007, *The Astrophysical Journal*, 668, 1232
- Filippov B. P., 2020, *Astronomy Reports*, 64, 272
- Guo Y., Cheng X., Ding M., 2017, *Science China Earth Sciences*, 60, 1408
- Hassanin A., Kliem B., 2016, *The Astrophysical Journal*, 832, 106
- Hassanin A., Kliem B., Seehafer N., Török T., 2022, *The Astrophysical Journal Letters*, 929, L23
- Hood A. W., Priest E. R., 1979, *Solar Physics*, 64, 303
- Hood A. W., Priest E. R., 1981, *Geophysical & Astrophysical Fluid Dynamics*, 17, 297
- Ji H., Wang H., Schmahl E. J., Moon Y.-J., Jiang Y., 2003, *The Astrophysical Journal*, 595, L135
- Jiang C., Wu S. T., Yurchyshyn V., Wang H., Feng X., Hu Q., 2016, *The Astrophysical Journal*, 828, 62
- Jiang C., et al., 2021, *Nature Astronomy*, 5, 1126
- Kliem B., Török T., 2006, *Physical Review Letters*, 96, 255002
- Liu R., 2020, *Research in Astronomy and Astrophysics*, 20, 165
- Luo R., Liu R., 2022, *The Astrophysical Journal*, 929, 2
- Moore R. L., Sterling A. C., Hudson H. S., Lemen J. R., 2001, *The Astrophysical Journal*, 552, 833
- Patsourakos S., et al., 2020, *Space Science Reviews*, 216, 131
- Sun X., et al., 2015, *The Astrophysical Journal*, 804, L28
- Titov V. S., Démoulin P., 1999, *Astronomy & Astrophysics*, 351, 707
- Török T., Kliem B., 2005, *The Astrophysical Journal*, 630, L97
- Török T., Kliem B., Titov V. S., 2004, *Astronomy & Astrophysics*, 413, L27
- Török T., Berger M. A., Kliem B., 2010, *Astronomy and Astrophysics*, 516, A49
- Zhou Z., Cheng X., Zhang J., Wang Y., Wang D., Liu L., Zhuang B., Cui J., 2019, *The Astrophysical Journal Letters*, 877, L28
- Zhou Z., Jiang C., Liu R., Wang Y., Liu L., Cui J., 2022, *The Astrophysical Journal Letters*, 927, L14
- Zhou Z., Jiang C., Yu X., Wang Y., Hao Y., Cui J., 2023, *Frontiers in Physics*, 11, 1119637
- Zuccarello F. P., Aulanier G., Gilchrist S. A., 2015, *The Astrophysical Journal*, 814, 126

This paper has been typeset from a $\text{\TeX}/\text{\LaTeX}$ file prepared by the author.